Analytical Methods

This article can be cited before page numbers have been issued, to do this please use: S. Ghosal, P. K. Weber and A. Laskin, *Anal. Methods*, 2014, DOI: 10.1039/C3AY42012D.

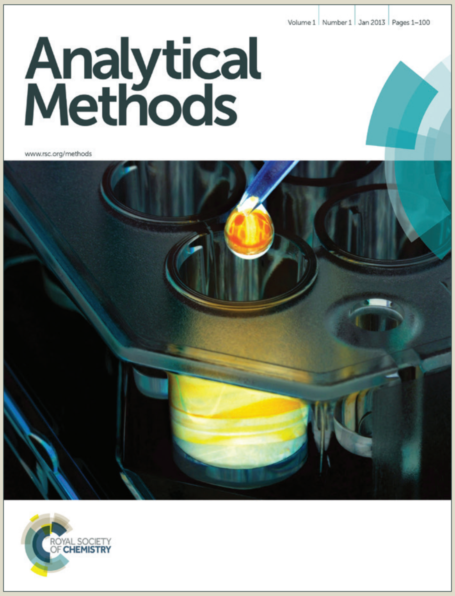

ROYAL SOCIETY OF CHEMISTRY

www.rsc.org/methods

View Article Online
DOI: 10.1039/C3AY42012D

# Spatially resolved chemical imaging of individual atmospheric particles using nanoscale imaging mass spectrometry: Insights into particle origin and chemistry

Sutapa Ghosal[1],*, Peter Weber[2], Alexander Laskin[3]

[1]*Environmental Health Laboratory, California Department of Public Health, Richmond, CA 94804*

[2]*Glenn T. Seaborg Institute, Lawrence Livermore National Laboratory, Livermore, CA 94550*

[3]*William R. Wiley Environmental Molecular Sciences Laboratory, Pacific Northwest National Laboratory, Richland, WA 99352*

**KEYWORDS** particle analysis, NanoSIMS, internally mixed particles.

Manuscript in preparation for submission to

*Analytical Methods*

January 2014

***Corresponding Author**

Sutapa Ghosal
Sutapa.Ghosal@cdph.ca.gov

View Article Online
DOI: 10.1039/C3AY42012D

## Abstract

Knowledge of the spatially resolved composition of atmospheric particles is essential for differentiating between their surface versus bulk chemistry and understanding particle reactivity and the potential environmental impact. We demonstrate the application of nanometer-scale secondary ion mass spectrometry (CAMECA NanoSIMS 50 ion probe) for 3D chemical imaging of individual atmospheric particles without any sample pre-treatment, such as the sectioning of particles. Use of NanoSIMS depth profile analysis enables elemental mapping of particles with nanometer spatial resolution over a broad of range of particle sizes. We have used this technique to probe spatially resolved composition of ambient particles collected during a field campaign in Mexico City. Particles collected during this campaign have been extensively characterized in the past using other particle analysis techniques and hence offer a unique opportunity for exploring the utility of depth-resolved chemical imaging in ambient particle research.[1] Particles examined in this study include those collected during a pollution episode related to urban waste incineration as well as background particles from the same location before the episode. Particles from the pollution episode show substantial intra-particle compositional variability typical of particles resulting from multiple emission sources. In contrast, the background particles have relatively homogeneous compositions with enhanced presence of nitrogen, oxygen, and chlorine at the particle surface. The observed surface enhancement of nitrogen and oxygen species is consistent with the presence of surface nitrates resulting from gas-particle heterogeneous interactions and is indicative of atmospheric ageing of the particles. The results presented here illustrate 3D characterization of ambient particles for insights into their chemical history.

View Article Online
DOI: 10.1039/C3AY42012D

# INTRODUCTION

Atmospheric aerosols originating from natural and anthropogenic sources constitute an integral part of the atmosphere. Aerosols have direct and indirect impact on air quality, climate, and human health. However, the exact mechanisms and scale of these effects are not well understood because of the range of variability and complexity associated with aerosols.[2] Aerosols consist of a complex mixture of organic and inorganic species. Furthermore, chemical composition of individual aerosol particles is often heterogeneous both over particle surface and as a function of depth (i.e., the surface composition being different from the bulk composition of particles). Several studies have indicated that, in fact, particle surfaces govern important processes in atmospheric chemistry and physics of aerosols, such as the ability of particles to function as cloud condensation nuclei (CCN).[3, 4] Information regarding chemical heterogeneity at the individual particle level; that is, the chemical mixing state, combined with information on particle size, is essential for understanding and predicting the reactivity, environmental, and health impacts of aerosols. Moreover, particular chemicals associated with certain particle types often enable identification of their unique emission sources. Hence, definitive understanding of the environmental impact of aerosols, and identification of their sources, requires knowledge of the size and spatially resolved chemical speciation of individual particles.[3, 5]

A number of analytical approaches have been adopted for characterizing individual particles. While methods of mass spectrometry[6-9] have become the most commonly used characterization tool in this respect, other techniques include electron microscopy and X-ray microanalysis,[10, 11] X-ray spectromicroscopy,[12] and laser-induced breakdown spectroscopy.[13] For instance, high-

View Article Online
DOI: 10.1039/C3AY42012D

resolution transmission electron microscopy (HRTEM) combined with electron-beam-based spectroscopies have been used for element-specific chemical imaging along with structural and elemental characterization.[11] Similarly, scanning transmission X-Ray microscopy with near-edge X-ray absorption fine structure (STXM-NEXAFS) has been used to probe morphology and functional group composition of submicron aerosol particles.[12] While these techniques offer highly sensitive chemical analysis with nanometer-scale lateral resolution, they are limited to the analyses of submicron size particles that are sufficiently transparent to the electron beam and hence do not offer direct depth-specific chemical information. Typically, microscopy techniques integrate chemical information over the entire radiation pathway and therefore provide limited depth-resolved speciation of the particle interior. Access to interior structural and compositional information for submicron particles by these techniques requires sectioning of the particles to reveal their interior structure for analyses.[14, 15] For instance, Chen et al. have demonstrated application of FIB/SEM (a dual-beam focused ion beam/scanning electron microscope) for ion beam milling and microanalysis of fly ash particles.[15] An analytical approach that offers spatially resolved compositional information for a broad range of particle sizes without requiring prior sample preparation procedures will be an important addition to existing aerosol analytical capabilities.

Secondary ion mass spectrometry (SIMS), a well-established surface characterization tool, has been used successfully for spatially resolved chemical imaging in a variety of inorganic and organic samples.[16-18] SIMS is capable of sub-micrometer depth resolution and thus offers access to detailed depth-specific compositional information without requiring sample sectioning.[19] Moreover, SIMS can detect elemental and molecular ions and is suitable for quantitative isotope

View Article Online
DOI: 10.1039/C3AY42012D

ratio measurements as well. While SIMS-based depth profile analysis is a well-established technique, the broad variability in dimensions and the complexity of atmospheric particles can pose significant analytical challenges. Atmospheric particles can range in size from 1 nm up to 10 µm, which corresponds to a mass range of $10^{-21}$ g to $10^{-9}$ g, respectively.[2] Characterizing such a broad range of particles, especially ones with small dimensions, requires a highly focused ion beam that is not standard in conventional SIMS instruments, which typically have lateral resolution >1000 nm.[20] The CAMECA NanoSIMS 50 ion probe is a relatively recent advance in dynamic SIMS technology that enables chemical mapping with nanometer-scale lateral (~50 nm) and depth resolution, using a focused beam of $Cs^+$ primary ions.[20] The NanoSIMS instrument provides >10 higher sensitivity at high mass resolving power (3000 to 10,000 $m/\Delta m$) compared to conventional SIMS instruments. Collection efficiency of this instrument, also known as useful yield, can be as high as 8% for O,[21] which is essential for characterizing small volumes associated with individual atmospheric particles. It is equipped with a suite of five detectors for simultaneous collection of up to five different secondary ions, which enables precise and efficient measurements in small sample volumes.

We have previously used NanoSIMS imaging depth profile analyses to successfully characterize individual bacterial spores, and model organic aerosols along with their reaction products.[22, 23] NanoSIMS depth resolution in these experiments was determined to be <10.5 nm, based on the analysis of a silicon-carbon multilayer sample of known dimensions.[22] These studies demonstrated the feasibility of 3D characterization of complex, micron-scale single particles using this methodology. In the case of model secondary organic aerosol (SOA), depth-resolved characterization revealed an increase in O content as a function of depth into SOA following

View Article Online
DOI: 10.1039/C3AY42012D

ozonolysis.[23] The observed depletion of O at the particle surface relative to its bulk suggested that the hydrophilic -COOH products of ozonolysis were likely buried away from the air/particle interface thus making the SOA surface hydrophobic. This has important implications for the SOAs' ability to act as CCN. Additionally, other studies have used NanoSIMS for the quantitative analysis of sulfur isotopes in individual particles, a well-established methodology for characterizing sources and the fate of sulfur in the atmosphere.[24-27]

In this report, we present the application of NanoSIMS-based chemical imaging for characterizing atmospheric particles collected during a field study, Megacity Initiative: Local and Global Research Observations (MILAGRO), held March 2006 in the Mexico City metropolitan area (MCMA) (see http://mce2.org/).[28] The MILAGRO study employed a suite of complementary analytical techniques for detailed investigation of the chemistry, size, morphology, metal speciation, and mixing state of metal-containing particles sampled during the study.[1, 29, 30] Given the extensive information already available from previously published reports, the MILAGRO particle samples provided a unique opportunity for exploring the utility of this type of analysis. The primary objective of this study is to access spatially resolved compositional information at the individual particle level for insights into the origin and subsequent atmospheric reactivity of aerosols. We have used depth profile analyses to map the lateral and depth-resolved distribution of relevant ions in individual particles sampled during two distinct time periods. The results presented here reveal unique trends in particle mixing states attributable to the origin and specific chemical history of the particles.

View Article Online
DOI: 10.1039/C3AY42012D

## EXPERIMENTAL SECTION

**Sampling site and particle collection.** The sampling site was situated in northern MCMA at the Instituto Mexicano del Petroleo (Mexican Institute of Petroleum), where the environment was frequently impacted by industrial, vehicular, and residential emissions.[29] Using compact time-resolved aerosol collectors (TRACs), particle samples were collected onto pre-arranged microscopy substrates that were replaced automatically every 15 minutes.[31, 32] Particles examined in this study were collected on Si-wafer chips during two different times, one corresponding to a characteristic episode of air pollution related to waste incineration, and the other preceding the pollution episode.[1] Specifically, particles related to the waste incineration episode were collected on March 24, 2006, at 4:45-5:00 a.m. Central Standard Time (CST), while the second sample was collected at 2:45-3:00 a.m. CST of the same day and represents typical background particles present in the air before the pollution episode. For clarity of presentation, we refer to these samples as S1 (background particles) and S2 (particles from the waste incineration episode). Corresponding samples of particles collected on TEM grids before and during this pollution episode have been previously characterized using computer-controlled scanning electron microscopy (CCSEM) with energy-dispersive X-ray analysis (EDX) and X-ray spectromicroscopy.[1]

**Secondary Ion Mass Spectrometry (SIMS) Analysis.** The particle samples were analyzed using the NanoSIMS 50 (CAMECA Instruments, Geneviers, France) instrument at Lawrence Livermore National Laboratory in April 2007. The instrument was set to simultaneous secondary ion collection mode with pulse counting on electron multipliers.[33] This enables simultaneous

View Article Online
DOI: 10.1039/C3AY42012D

collection of five elements or isotopes originating from the same sputtered volume of the sample. A micro-cesium source was used to generate $Cs^+$ primary ions, with impact energy of 16 kV for sample interrogation. The primary beam was stepped across the sample to produce element specific, quantitative digital images. The $Cs^+$ primary ion beam enhances the yield of electronegative elements and was used to analyze samples for $^{12}C^-$, $^{16}O^-$, $^{12}C^{14}N^-$, $^{32}S^-$, and $^{35}Cl^-$ ions. The lateral resolution of the secondary ion image is controlled by the primary beam spot size. For the detection of electronegative elements a 1- to 6-pA $Cs^+$ primary beam was focused to a nominal spot size between 100-200 nm and stepped over the sample in a 256- x 256-pixel raster to generate secondary ions. Dwell time was 1-7 ms/pixel, and raster area was between 6-100 $\mu m^2$. For depth profile analysis, secondary ion intensity data was collected as a function of sputter cycles. An increasing number of sputter cycles corresponds to increasing depth inside the particle. Using an experimentally determined sputter rate, one can translate the sputter cycle into an estimate of the sputtered depth. A previously determined sputter rate of 2.5 $nm \cdot \mu m^2/pA \cdot s$ was used to estimate the sputtered depth during depth profile analyses of the particles.[22] The mass spectrometer was tuned for ~3000 $m/\Delta m$ mass resolving power. NanoSIMS is an ultra-high vacuum (UHV) technique, so samples were kept under UHV conditions (1 x $10^{-10}$ Torr) during analysis.

Data were processed as quantitative elemental images using custom software (L’image, L.R. Nittler, Carnegie Institution of Washington) and were corrected for detector dead time and image shift during analysis. To account for any systematic signal intensity variations during the measurements, the NanoSIMS secondary ion intensities were normalized to selected ion ($^{12}C^-$) intensity.

View Article Online
DOI: 10.1039/C3AY42012D

## RESULTS AND DISCUSSION

On March 24, 2006, aerosol time-of-flight mass spectrometry (ATOFMS) measurements identified a period (~4:00-6:00 a.m. CST) with a high abundance of Zn- and Pd-containing particles at this particular sampling site.[1] This event was representative of similar episodes that were frequently observed at this location, approximately at the same time of day. Previously, Moffet et al. have presented detailed characterization of the bulk composition, size, and morphology of particles sampled during this particular episode.[1] Based on their observations, they concluded that urban waste incineration was the primary source of these internally mixed Pb-Zn-Cl particles. They also discussed the potential conversion of chlorides in these particles to nitrates via heterogeneous interaction with gas-phase nitric acid.[1] We have used NanoSIMS to characterize individual particles collected before and during this pollution episode. The goal is to identify compositional characteristics that distinguish particles from these two time periods. Moreover, depth-resolved compositional information afforded by NanoSIMS analysis can potentially offer insights into the atmospheric processing of particles. We measured intra- and inter-particle distributions of $^{12}C^-$, $^{16}O^-$, $^{12}C^{14}N^-$, $^{32}S^-$, and $^{35}Cl^-$ ions, as these ions are potential indicators of the origin and subsequent atmospheric processing of the particles; for example, the heterogeneous interaction of particle chlorides with gas-phase nitric acid. Heterogeneous interactions occur at the gas/particle interface, hence the particle surface composition is expected to represent the products of its recent heterogeneous processing; for example, enhancement of nitrate at the particle surface relative to the bulk. The distinct compositional characteristics of particles from the two sampling periods are presented below.

DOI: 10.1039/C3AY42012D

**Comparison of mixing states of background (S1) versus pollution episode (S2) particles.** The overall elemental composition of S1 and S2 particles are shown in Figure 1, which presents their respective ion intensity maps. The pollution episode sample (S2) has overall greater abundance of particles, including those containing Cl, compared to the background sample (S1). Table 1 tabulates the number of observed particles in each elemental category for the two samples. Each particle typically consists of multiple elements. Figure 1 and Table 1 show that the two samples are distinct both in terms of the overall abundance of particles and mixing state of the individual particles. Figure 2 shows a series of $^{12}C^-$ ion images of the S2 sample: total $^{12}C^-$ image (Figure 2a), $^{12}C^-$ ion intensity map representing $^{12}C^-$ ion intensities > 30% (Figure 2b), and $^{12}C^-$ ion intensity map showing regions where the only detectable species were $^{12}C^-$ (Figure 2c). Some of the larger particles are shown to have amorphous regions dominated by the presence of $^{12}C^-$. Abundance of $^{12}C^-$ along with the amorphous morphology of these regions, as seen in Figure 2c, are consistent with the presence of elemental carbon (EC) and suggest combustion-related origin of these particles. Overall, the presence of EC and the higher abundance of Cl-containing particles suggest an influx of particles from a combustion source such as an incinerator. These observations are in agreement with previous studies, which have reported peaks in Zn-, Pb-, and Cl-containing particles from local industrial waste incineration during the early morning hours.[1]

**Background particles (S1):** Figure 3 shows total ion images and selected lateral ion profiles of S1 particles. Total ion images are generated from summed ion counts over the cumulative sputtering process. Fewer particles are observed during this sampling period compared to the S2

View Article Online
DOI: 10.1039/C3AY42012D

sample. S- and O-containing particles are the most abundant and are indicative of typical sulfate background particles (Figure 3a). In fact, all of the observed particles contain S and/or O and are frequently intermixed with C, N, and/or Cl. Particles with multiple elemental signatures are typically larger in size compared to particles containing only S and/or O. It is likely that the larger particles are the product of condensation growth of smaller sulfate particles, which often act as condensation nuclei for ambient species. Cl-containing particles are sparse during this period. Overall, particles show laterally homogeneous distribution of the probed ions (Figure 3b-c).

Figure 4 presents depth-profile analyses of typical S1 particles, showing $^{12}C^-$ and $^{32}S^-$ total ion images as well as plots of ion intensities as a function of the estimated sputtered depth. Two particles are identified in the total ion images as particle 1 (a relatively small particle containing primarily $^{32}S^-$ and $^{16}O^-$), and particle 2 (a larger particle containing $^{12}C^-$ and $^{14}N^-$ in addition to $^{32}S^-$ and $^{16}O^-$). Ion intensity plots in Figure 4b show both the absolute and normalized (relative to $^{12}C^-$) ion intensities as a function of sputter depth for particles 1 and 2. The dashed lines indicate the sputtered depths at which the $^{32}S^-$ (particle 1) or $^{12}C^-$ (particle 2) ion intensity drops to 50% of its maximum value, which, based on experimental observations, is expected to represent the particle/substrate interface. Particle 1, which shows relatively homogeneous distribution of $^{32}S^-$ and $^{16}O^-$ as a function of depth, is likely a sulfate particle. In comparison, the larger particle 2 has a layered composition with enhanced presence of $^{14}N^-$ and $^{16}O^-$ at the surface and $^{32}S^-$ and $^{16}O^-$ dominating its interior. The observed compositional profile of particle 2 is indicative of a particle with a sulfate core surrounded by N- and O-containing coating. Particles 1 and 2 show similar $^{35}Cl^-$ depth profiles, with enhancement of $^{35}Cl^-$ at the particle surface.

View Article Online
DOI: 10.1039/C3AY42012D

The layered composition of particle 2 is indicative of a particle that has undergone atmospheric processing with the surface composition reflecting the products of its most recent heterogeneous interaction. For instance, co-location of N and O at the particle surface is consistent with the presence of surface nitrate species, potentially a product of the heterogeneous interaction of particle chlorides with gas-phase nitric acid.[34] Gaseous hydrogen chloride (HCl), another product of this reaction, has been shown to re-deposit on neighboring particles and hence is a potential source of the surface-enhanced Cl.[1, 35]

As mentioned earlier, the larger S- and O-containing particles, which also contain C and N, are likely to have originated from sulfate particles via condensation of ambient species over time. Hence, surface compositions of such particles will be dominated by the condensed species, while the core will consist of sulfate. This view is supported by the results shown in Figure 5, which compares the spatial distributions of $^{12}C^-$ and $^{32}S^-$ ions in one such particle. Figure 5a and b show ion maps of the overall $^{12}C^-$ distribution, and the areal difference between $^{12}C^-$ and $^{32}S^-$ distributions in the particle, respectively. The ring structure representing the areal difference between $^{12}C^-$ and $^{32}S^-$ distributions in the particle (Figure 5b) suggests a sulfate particle with condensed organic species on the surface, a result of particle ageing. These observations are in agreement with a previous study, which concluded that sulfate- and organic-containing aerosols observed during this time were aged emissions transported from the Tula refinery complex located ~120 km north of the sampling site.[29]

View Article Online
DOI: 10.1039/C3AY42012D

**Waste incineration particles (S2):** The pollution episode sample (S2) has a greater abundance of particles as well as significant compositional heterogeneity at the intra- and inter-particle level in comparison to the background sample discussed above. Figure 6 shows the total ion images for this sample. S- and O-containing particles appear to be the most abundant types, and they frequently include C and N species. C, N, and Cl appear to coexist in many of the particles. Greater abundance of particles in the sample and the predominance of S- and O-containing species are characteristics of this pollution episode.[1]

Moffet et al. have reported the presence of metal-containing (Pb, Zn) inorganic inclusions typically located in the particle interior during this particular pollution episode.[29] Based on their observations, they concluded that the inorganic inclusions were predominantly metal nitrate and/or metal oxide species. While we did not analyze for metal ions in this study, we can indirectly infer the presence of these inclusions in some of the particles based on depth-resolved distributions of the analyzed ions. Figure 7 shows lateral and depth-resolved ion profiles of two S2 particles. In contrast to S1 particles (Figure 4), the S2 show localized enhancement of nitrogen and oxygen species in the interior (Figures 7d-e), which is consistent with the presence of centrally located metal nitrate and/or metal oxide inclusions. In addition to the potential presence of metal inclusions, S2 particles show significant overall compositional heterogeneity with respect to the analyzed ions. The intra-particle heterogeneity associated with these particles is distinct from that of the background particles, discussed previously. S2 particles appear to be a complex mixture of various constituents without any discernible compositional pattern.  These observations support previous studies, which have concluded that particles resulting from incineration related emissions have greater compositional heterogeneity compared to background

View Article Online
DOI: 10.1039/C3AY42012D

particles, which are typically homogenized over time via atmospheric processing.[29] Greater abundance of Cl-containing particles observed during this episode is also consistent with waste incineration being the likely source of these particles.[1] In addition to waste incineration, this particular sampling site was impacted by a number of other emission sources, including heavy vehicular traffic, which likely contributed to the particle chemistry as well.

In this study we have used NanoSIMS chemical imaging and depth profile analyses of individual atmospheric particles for insights into their origin and reactive history. Particles from the waste incineration episode (S2) display significant intra-particle compositional heterogeneity and higher Cl content, both of which are consistent with an influx of freshly emitted particles from combustion-related sources. Urban background particles sampled before the pollution episode (S1) show distinct depth dependent compositional profiles, suggestive of atmospheric ageing of particles over their extended lifetime. Typically, the surface of an aged particle contains the products of its most recent atmospheric processing. A particular advantage of the present analytical approach compared to conventional methods of aerosol analyses is that it offers direct access to spatially resolved (lateral and depth) chemical composition of individual particles. For instance, depth profile analyses of background particles presented here reveal the surface localization of N-, O- and Cl-containing species surrounding a sulfate core. This depth-dependent compositional profile is consistent with the ageing of particles via heterogeneous transformation of chlorides to nitrates at the particle surface. In contrast, freshly generated waste incineration particles are distinguished by their complex lateral and depth-resolved compositional heterogeneity. The results presented here illustrate the feasibility and potential

View Article Online
DOI: 10.1039/C3AY42012D

advantages of spatially resolved chemical imaging (using NanoSIMS) in aerosol research; further work needs to be done to fully explore its capability.

## Acknowledgments

AL acknowledges support by the Chemical Imaging Initiative under the Laboratory Directed Research and Development funds of Pacific Northwest National Laboratory (PNNL). This work was performed under the auspices of the U.S. Department of Energy at Lawrence Livermore National Laboratory under Contract DEAC52-07NA27344.

View Article Online
DOI: 10.1039/C3AY42012D

**References:**

1. R. C. Moffet, Y. Desyaterik, R. J. Hopkins, A. V. Tivanski, M. K. Gilles, V. Shutthanandan, L. T. Molina, R. A. Gonzalez, K. S. Johnson, M. J. Molina, A. Laskin and K. A. Prather, *Environmental Science and Technology*, 2008, **42**, 7091–7097.
2. K. A. Prather, C. D. Hatch and V. H. Grassian, *Annu. Rev. Anal. Chem.*, 2008, **1**, 485–514.
3. A. R. Ravishankara, *Science*, 1997, **276**, 1058-1065.
4. E. M. Knipping, M. J. Lakin, K. L. Foster, P. Jungwirth, D. J. Tobias, R. B. Gerber, D. Dabdub and B. J. Finlayson-Pitts, *Science*, 2000, **288**, 301.
5. B. J. Finlayson-Pitts and J. N. Pitts, *Science*, 1997, **276**, 1045-1052.
6. K. A. Pratt and K. A. Prather, *Mass Spectrom. Rev.* , 2012, **31**, 1-16.
7. K. A. Pratt and K. A. Prather, *Mass Spectrom. Rev.* , 2012, **31**, 17-48.
8. A. Laskin, J. Laskin and S. A. Nizkorodov, *Environmental Chemistry*, 2012, **9**, 163-189.
9. J. Laskin, A. Laskin and S. A. Nizkorodov, *International Reviews in Physical Chemistry*, 2013, **32**, 128-170.
10. A. Laskin, in *in Fundamentals and Applications in Aerosol Spectroscopy*, eds. R. Signorell and J. Reid, CRC Press Taylor and Francis Group, Boca Raton, FL, 2010, pp. 463-491.
11. M. Posfai and P. R. Buseck, *Annu. Rev. Earth Planet. Sci.*, 2010, **38**, 17–43.
12. R. C. Moffet, A. V. a. Tivanski and M. K. Gilles, in *Fundamentals and Applications in Aerosol Spectroscopy*, eds. R. Signorell and J. Reid, Taylor and Francis Books, Inc, 2010, pp. 419–462.

View Article Online
DOI: 10.1039/C3AY42012D

13. G. A. Lithgow, A. L. Robinson and S. G. Buckley, *Atmos. Environ.*, 2004, **38**, 3319–3328.

14. J. M. Conny and G. A. Norris, *Environ. Sci. Technol.*, 2011, **45**, 7380–7386.

15. H. Chen, V. H. Grassian, L. V. Saraf and A. Laskin, *Analyst* 2013, **138**, 451-460.

16. J. Goschnick, M. Fichter, M. Lipp, J. Schuricht and H. Ache, *J. Appl. Surf. Sci.*, 1993, **70**, 63-67.

17. W. Jambers, L. De Bock and R. Van Grieken, *Analyst* 1995, **120**, 681-692.

18. R. E. Peterson and B. E. Tyler, *Applied Surface Science*, 2003, **751-756**, 203-204.

19. R. G. Wilson, F. A. Stevie and C. W. Magee, *Secondary Ion Mass Spectrometry: A Practical Handbook for Depth Profiling and Bulk Impurity Analysis*, Wiley, New York, 1989.

20. F. Hillion, B. Daigne, F. Girard and G. Slodzian, in *Secondary Ion Mass Spectrometry: SIMS IX*, eds. A. Benninghoven, Y. Nihei, R. Shimizu and H. W. Werner, Wiley, New York, 1993, pp. 254–257.

21. G. Slodzian, F. Hillion, F. J. Stadermann and F. Horreard, *Applied Surface Sceince* 2003, **203-204** 789-801.

22. S. Ghosal, S. J. Fallon, T. J. Leighton, K. E. Wheeler, M. l. J. Kristo, I. D. Hutcheon and P. K. Weber, *Analytical Chemistry* 2008, **80**, 5986.

23. T. M. McIntire, O. S. Ryder, P. L. Gassman, Z. Zhu, S. Ghosal and B. J. Finlayson-Pitts, *Atmospheric Environment* 2010, **44**, 939-944.

24. E. Harris, B. Sinha, S. Foley, J. N. Crowley, S. Borrmann and P. Hoppe, *Atmos. Chem. Phys.*, 2012, **12**, 4867.

View Article Online
DOI: 10.1039/C3AY42012D

25. E. Harris, B. Sinha, P. Hoppe, J. N. Crowley, S. Ono and S. Foley, *Atmospheric Chemistry and Physics* 2012, **12**, 407- 423.

26. B. Winterholler, P. Hoppe, S. Foley and M. O. Andreae, *International Journal of Mass Spectrometry.*, 2008, **272**, 63-77.

27. E. Harris, B. Sinha, D. van Pinxteren, A. Tilgner, K. W. Fomba, J. Schneider, A. Roth, T. Gnauk, B. Fahlbusch, S. Mertes, T. Lee, J. Collett, S. Foley, S. Borrmann, P. Hoppe and H. Herrmann, *Science*, 2013, **340**, 727-730.

28. L. T. Molina, S. Madronich, J. S. Gaffney, E. Apel, B. de Foy, J. Fast, R. Ferrare, S. Herndon, J. L. Jimenez, B. Lamb, A. R. Osornio-Vargas, P. Russell, J. J. Schauer, P. S. Stevens, R. Volkamer and M. Zavala, *Atmospheric Chemistry and Physics*, 2010, **10**, 8697-8760.

29. R. C. Moffet, T. R. Henn, A. V. Tivanski, R. J. Hopkins, Y. Desyaterik, A. L. D. Kilcoyne, T. Tyliszczak, J. Fast, J. Barnard, V. Shutthanandan, S. S. Cliff, K. D. Perry, A. Laskin and M. K. Gilles, *Atmos. Chem. Phys.*, 2010, **10**, 961–976.

30. A. C. Aiken, D. Salcedo, M. J. Cubison, J. A. Huffman, P. F. DeCarlo, I. M. Ulbrich, K. S. Docherty, D. Sueper, J. R. Kimmel, D. R. Worsnop, A. Trimborn, M. Northway, E. A. Stone, J. J. Schauer, R. Volkamer, E. Fortner, B. de Foy, J. Wang, A. Laskin, V. Shutthanandan, J. Zheng, R. Zhang, J. Gaffney, N. A. Marley, G. Paredes-Miranda, W. P. Arnott, L. T. Molina, G. Sosa and J. L. Jimenez, *Atm. Chem. Phys.*, 2009, **9**, 6633-6653.

31. A. Laskin, M. J. Iedema and J. P. Cowin, *Aerosol Sci. Technol.*, 2003, **37**, 246-260.

32. A. Laskin, J. P. Cowin and M. J. Iedema, *J. Electron Spectrosc. Relat. Phenom.*, 2006, **150**.

33. R. Castaing and G. Slodzian, *J. Microsc.* , 1962, **1**, 31-38.

View Article Online
DOI: 10.1039/C3AY42012D

34. H. C. Allen, J. M. Laux, R. Vogt, B. J. Finlayson-Pitts and J. C. Hemminger, *The Journal of Physical Chemistry*, 1996, **100**, 6371-6375.

35. R. C. Sullivan, S. A. Guazzottia, D. A. Sodemana, Y. Tang, G. R. Carmichael and K. A. Prather, *Atmospheric Environment*, 2007, **41**, 7166–7179.

View Article Online
DOI: 10.1039/C3AY42012D

## Figure Captions

**Figure 1.** NanoSIMS-based ion intensity maps of (a) background sample, S1, and (b) waste incineration sample S2. The bright spots represent locations where the corresponding ion intensity is >30%.

**Table 1.** Number of detected particles in each elemental category. Each particle typically contains multiple elements. The numbers within the parentheses represent the observed size range for the particles.

**Figure 2.** Identification of elemental carbon using NanoSIMS ion intensity maps. (a) Measured $^{12}$C secondary ion distribution corresponding to S2 particles. Processed ion intensity maps showing (b) the distribution of $^{12}$C ion intensities greater than 30%, and (c) regions containing predominantly $^{12}$C ion; other ions are undetectable.

**Figure 3**. NanoSIMS characterization of background particles (S1). (a) Secondary ion images showing the lateral distribution of ions in the particles. (b) and (c) Lateral profiles showing the distributions of ions across the surface of two particles, which are identified in the $^{16}$O secondary ion image by lines representing the locations of the line-scan analysis.

**Figure 4.** NanoSIMS depth profile analysis of background particles (S1). (a) Total secondary ion images showing the lateral distribution of $^{12}$C and $^{32}$S ions. (b) and (c) Absolute and normalized (relative to $^{12}$C) depth-resolved distributions of ions corresponding to particles 1 and 2 identified by white squares in (a), respectively. The dashed vertical lines identify the sputtered depths at

View Article Online
DOI: 10.1039/C3AY42012D

which the $^{12}$C ion intensities drop to 50% of their maximum values and typically represent the particle/substrate interface.

**Figure 5.** NanoSIMS ion intensity maps of a particle showing the presence of carbon coating over sulfur core. (a) $^{12}$C ion intensity map, and (b) ion intensity map showing the difference between $^{12}$C and $^{32}$S, where the bright ring corresponds to the region containing $^{12}$C and not $^{32}$S.

**Figure 6.** NanoSIMS ion maps of the pollution episode sample (S2).

**Figure 7.** Lateral and depth-resolved compositional heterogeneity among particles from the pollution episode (S2). (a) $^{32}$S ion image with the lines depicting the line scan location for two individual particles (A and B). (b) and (c) Lateral profiles of particles A and B, respectively. (d) and (e) Depth profiles of particles A and B, respectively.

View Article Online
DOI: 10.1039/C3AY42012D

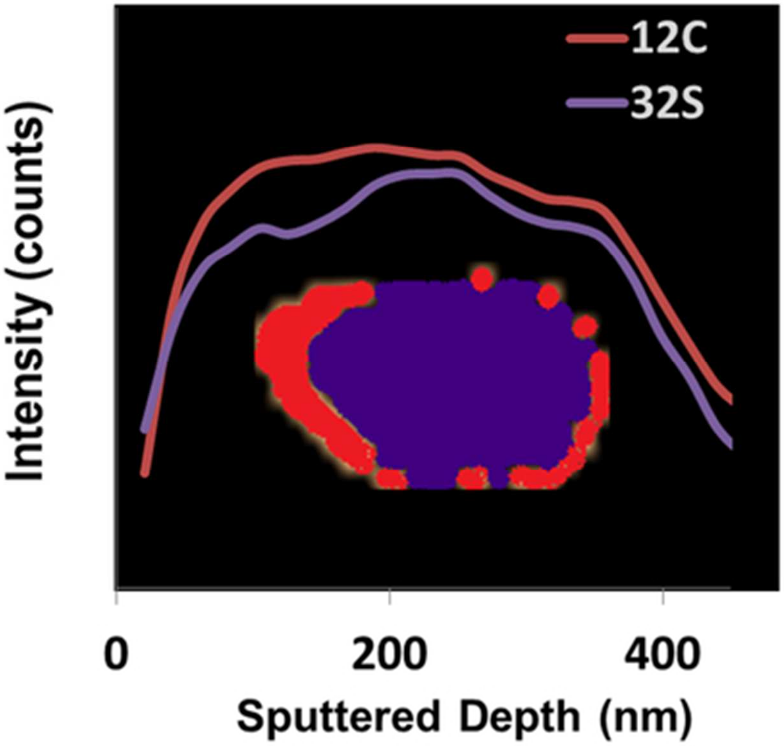

43x37mm (300 x 300 DPI)

View Article Online
DOI: 10.1039/C3AY42012D

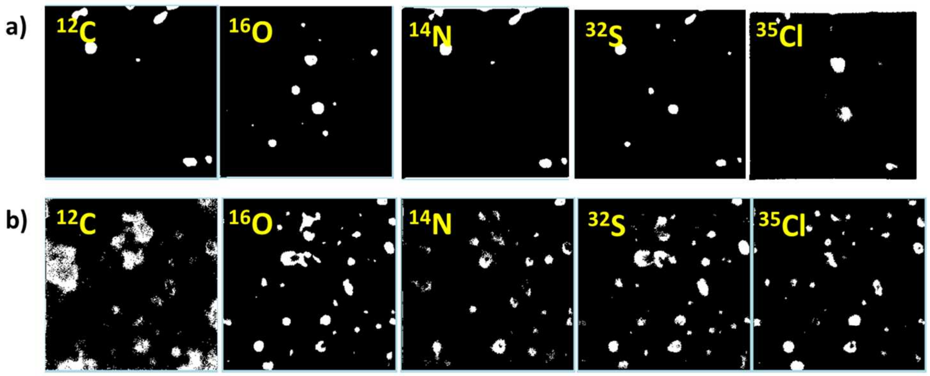

Figure 1. NanoSIMS-based ion intensity maps of (a) background sample, S1, and (b) waste incineration sample S2. The bright spots represent locations where the corresponding ion intensity is >30%.
237x105mm (150 x 150 DPI)

View Article Online
DOI: 10.1039/C3AY42012D

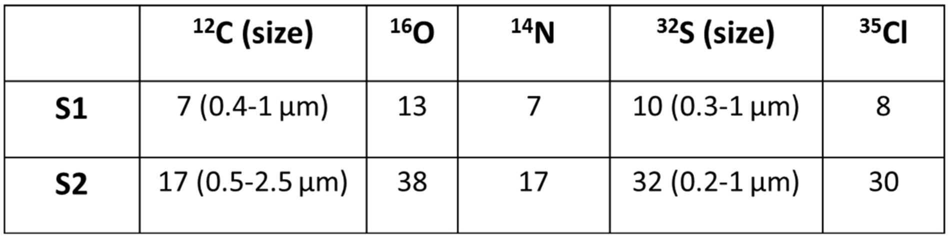

| | $^{12}C$ (size) | $^{16}O$ | $^{14}N$ | $^{32}S$ (size) | $^{35}Cl$ |
|---|---|---|---|---|---|
| **S1** | 7 (0.4-1 μm) | 13 | 7 | 10 (0.3-1 μm) | 8 |
| **S2** | 17 (0.5-2.5 μm) | 38 | 17 | 32 (0.2-1 μm) | 30 |

Table 1. Number of detected particles in each elemental category. Each particle typically contains multiple elements. The numbers within the parentheses represent the observed size range for the particles.
208x63mm (150 x 150 DPI)

View Article Online
DOI: 10.1039/C3AY42012D

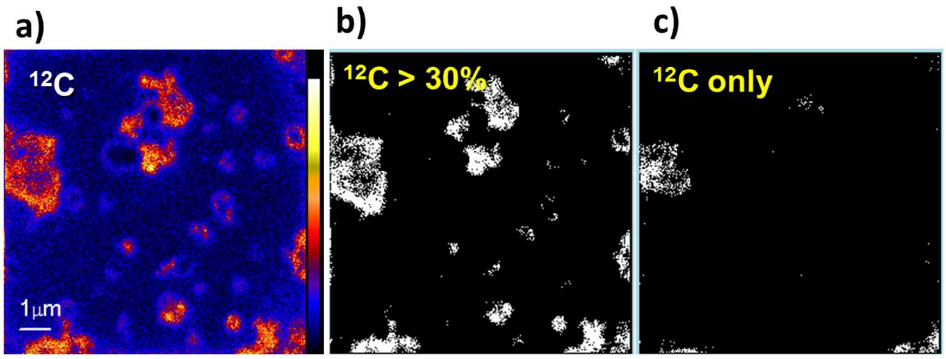

Figure 2. Identification of elemental carbon using NanoSIMS ion intensity maps. (a) Measured $^{12}$C secondary ion distribution corresponding to S2 particles. Processed ion intensity maps showing (b) the distribution of $^{12}$C ion intensities greater than 30%, and (c) regions containing predominantly $^{12}$C ion, other ions are undetectable.
224x90mm (150 x 150 DPI)

DOI: 10.1039/C3AY42012D

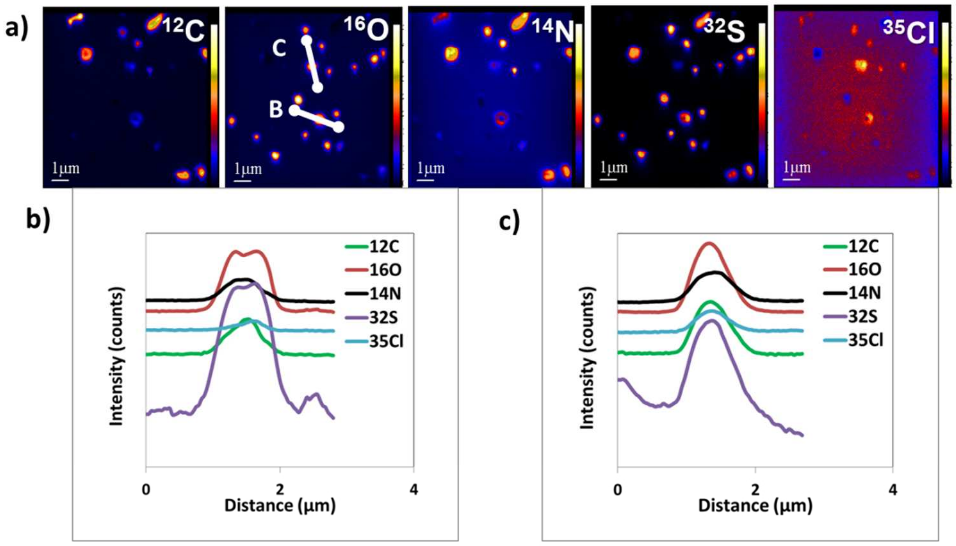

Figure 3. NanoSIMS characterization of background particles (S1). (a) Secondary ion images showing the lateral distribution of ions in the particles. (b) and (c) Lateral profiles showing the distributions of ions across the surface of two particles, which are identified in the $^{16}O$ secondary ion image by lines representing the locations of the line-scan analysis.
148x92mm (220 x 220 DPI)

View Article Online
DOI: 10.1039/C3AY42012D

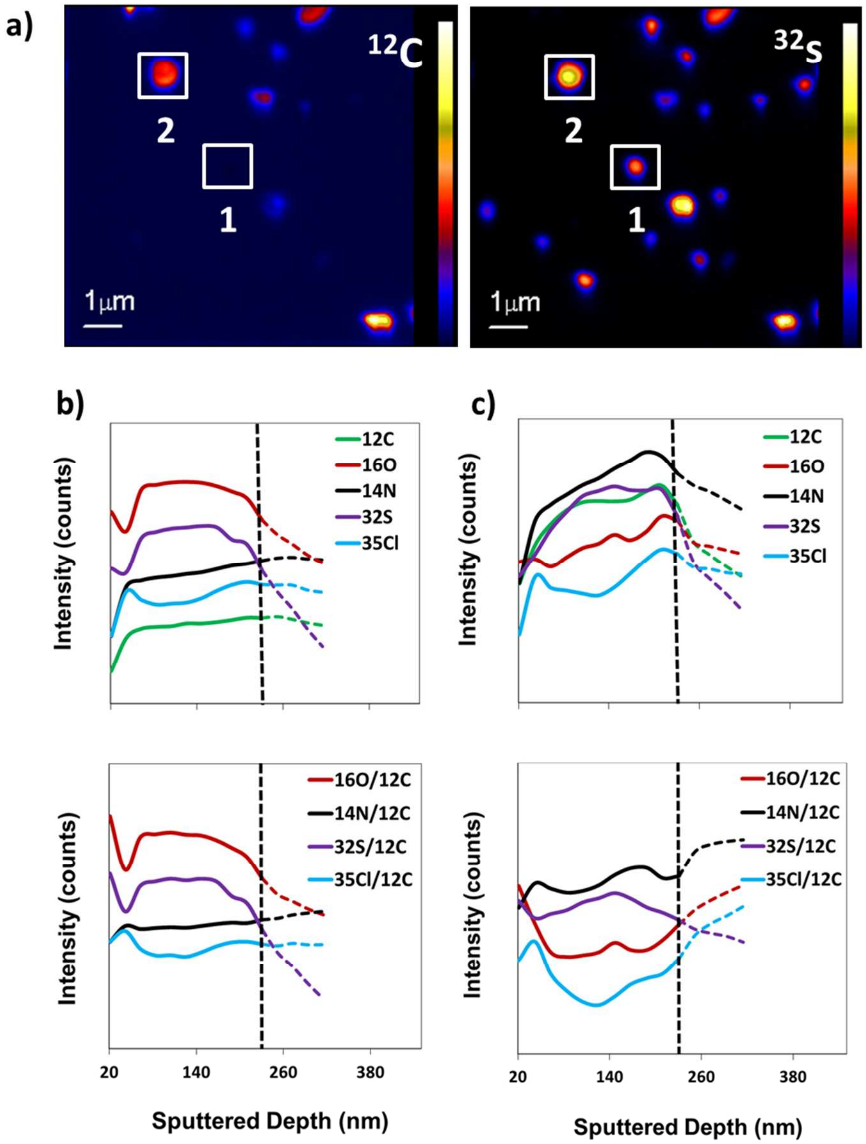

Figure 4. NanoSIMS depth profile analysis of background particles (S1). (a) Total secondary ion images showing the lateral distribution of $^{12}$C and $^{32}$S ions. (b) and (c) Absolute and normalized (relative to $^{12}$C) depth-resolved distributions of ions corresponding to particles 1 and 2 identified by white squares in (a), respectively. The dashed vertical lines identify the sputtered depths at which the $^{12}$C ion intensities drop to 50% of their maximum values and typically represent the particle/substrate interface.
182x219mm (150 x 150 DPI)

View Article Online
DOI: 10.1039/C3AY42012D

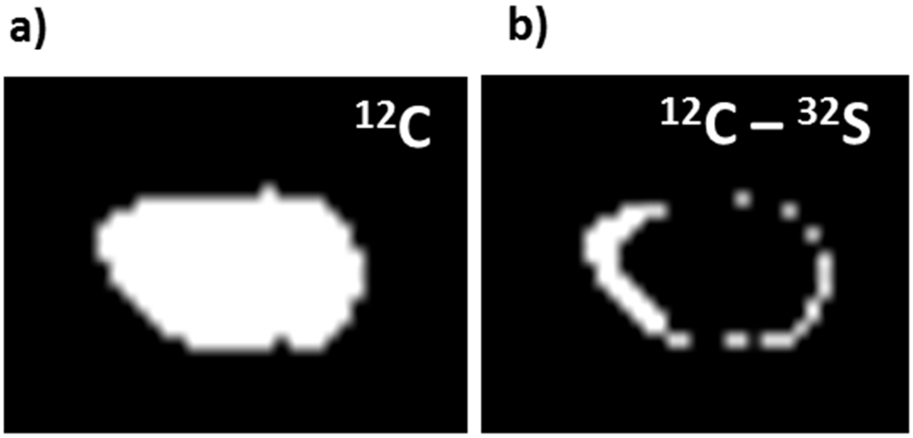

Figure 5. NanoSIMS ion intensity maps of a particle showing the presence of carbon coating over sulfur core. (a) $^{12}$C ion intensity map, and (b) ion intensity map showing the difference between $^{12}$C and $^{32}$S, where the bright ring corresponds to the region containing $^{12}$C and not $^{32}$S.
99x53mm (150 x 150 DPI)

View Article Online
DOI: 10.1039/C3AY42012D

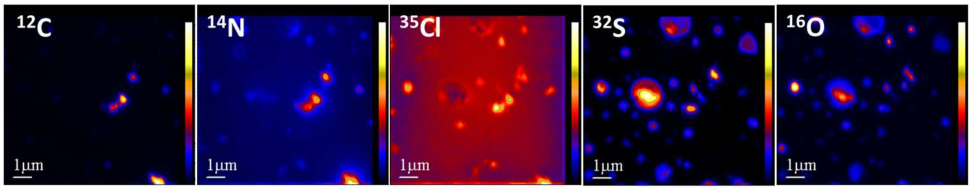

Figure 6. NanoSIMS ion maps of the pollution episode sample (S2).
270x55mm (150 x 150 DPI)

View Article Online
DOI: 10.1039/C3AY42012D

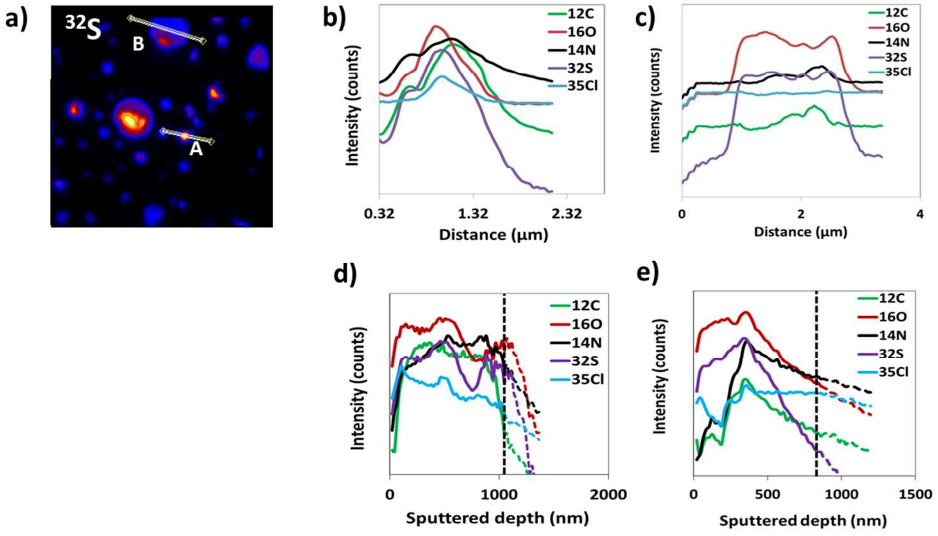

Figure 7. Lateral and depth resolved compositional heterogeneity among particles from the pollution episode (S2). (a) $^{32}$S ion image with the lines depicting the line scan location for two individual particles (A and B). (b) and (c) Lateral profiles of particles A and B, respectively. (d) and (e) Depth profiles of particles A and B, respectively.
219x124mm (150 x 150 DPI)